

Ocean model diagnosis of low frequency climate variability in the South Atlantic region

Frank Colberg, and C. J. C. Reason

Oceanography Department, University of Cape Town

Private Bag, Rondebosch 7701, South Africa

Abstract

South Atlantic Ocean variability is investigated by means of an ocean general circulation model (ORCA2), forced with the NCEP/ NCAR-reanalyses for the 1948-1999 period. A rotated EOF analysis of the mixed layer temperature suggests a breakdown of the South Atlantic into four subdomains, with characteristic spatial and temporal scales: (a) the tropical Atlantic, with mainly interannual fluctuations, (b) the northeastern subtropics, with variability on an interannual to decadal scale, (c) the midlatitudes, with interannual and multi-decadal variability and (d) the southwestern subtropics/ midlatitudes with a mixture of interannual and decadal variability. These modes are closely connected to anomalous atmospheric circulation patterns, which induce typical forcing mechanisms for each region.

Temperature changes in the western to central tropics are found to be driven by changes in surface heat fluxes and horizontal advection of heat, while in the central to eastern tropics and the northern Benguela region, temperature changes are connected to reduced vertical entrainment, altering the depth of the mixed layer and leading to reduced upwelling.

In the western and eastern subtropics, changes in the net surface fluxes drive the upper ocean temperature anomalies, and wind induced vertical mixing dissipate them, inducing changes in the depth of the mixed layer. Anomalous heat and volume transports are found to be related to anomalous Ekman and geostrophic currents in the eastern subtropics. A wind driven mechanism is suggested, whereby changes in Ekman related heat and volume transport lead to modulations of the subtropical gyre and thus to changes in the geostrophic related heat and volume transport.

Temporal variability in the midlatitudes is mainly due to horizontal advection and wind induced vertical mixing, whereby geostrophic advection of heat dominates in the western to central area, and Ekman induced heat transports are confined to the eastern midlatitudes.

1 Introduction

Over the last decade, an increasing number of studies have been devoted towards investigating South Atlantic climate variability. The need for an improved understanding of South Atlantic climate modes results from the important role that the South Atlantic Ocean plays in the context of the global climate system. The South Atlantic Ocean is unique in that it transports heat northwards across the equator, playing a major part in the thermohaline circulation (*Gordon, 1986; Schmitz, 1995*). On a regional scale, changes in sea surface temperature (SST) anomalies are found to impact on regional atmospheric circulation, leading to rainfall variability over the adjacent land masses (e.g. *Reason et al., 2002; Rouault et al., 2003; Robertson et al., 2003; Reason and Jagadheesha, 2005*).

Previous work on variability in the South Atlantic has focused on interannual to multi-decadal time scales (e.g. *Venegas et al., 1996, 1997, 1998; Reason, 2000; Reason et al., 2000, 2002; Wainer and Venegas, 2001; Palastanga et al., 2002, 2005; Colberg et al., 2004*). *Venegas et al. (1997)* examined the leading modes in the South Atlantic using 40 years of COADS SST and SLP. Their first coupled mode describes a decadal oscillation of the subtropical anticyclone that is accompanied by a north-south dipole structure in SST on the same time scale. The second mode involves an east-west shift of the anticyclone with fluctuations of 6-7 years in SST, whereas their third mode is associated with a north-south fluctuation of the subtropical high and SST anomalies in a latitudinal band in the central South Atlantic that shows a high correlation with ENSO. These findings are roughly similar to those of *Sterl and Hazeleger (2003)*, who analysed 52 years of NCEP/ NCAR-reanalyses. They found that anomalous atmospheric circulation patterns are mainly responsible for creating SST anomalies, as they induce changes in latent heat flux and anomalous mixed layer depth. The results of *Sterl and Hazeleger (2003)* have been confirmed by *Haarsma et al. (2005)*, who investigated the dominant leading modes of the South Atlantic with a hierarchy of coupled ocean-atmosphere models.

To date, relatively few attempts have been made to investigate South Atlantic

Ocean variability using model output. *Wainer and Venegas* (2001) analysed South Atlantic multi-decadal variability in the NCAR Climate System model in a 300 year integration model run and found significant oscillations of a 25-30 year period, which they associated with changes in the atmospheric circulation, that in turn affect the position of the Brazil Falkland/ Malvinas Current confluence zone, leading to changes in upper ocean temperatures there. The findings are in agreement with observational data, thus indicating that models are indeed useful in order to detect climate variability. Furthermore, models offer a more complete picture of what is happening in the oceans since they supply not only information about the surface but also allow investigation of sub-surface features such as Kelvin waves which are thought to be important for warm and cool events in the northern Benguela Current region (*Florenchie et al.*, 2003, 2004). The necessity of using model output in order to further understand South Atlantic variability has also been pointed out by *Sterl and Hazeleger* (2003). Only OGCMs can provide additional information on advective processes and baroclinic structures of the upper ocean. This information is vital in order to further understand the role of South Atlantic ocean variability in a global and regional climate context.

In the following, we use the ORCA2 OGCM to identify the leading modes of the South Atlantic upper ocean temperature and investigate in detail the physical processes, atmospheric forcing, heat and volume transports associated with these modes.

2 Model description

The OGCM used is the ORCA2 model, which is the global version of the Ocean Parallelise (*Madec et al.*, 1998). Its domain extends from 78°S to 90°N. Bottom topography is derived from *Smith and Sandwell* (1997) data complemented by values from the 5' \times 5' ETOPO 5 data set. Lateral mixing is oriented isopycnically, and the eddy parametrisation scheme of *Gent and McWilliams* (1990) is applied poleward of 10 degrees in both hemispheres. Vertical mixing is achieved using the TKE

scheme of *Blanke and Delecluse* (1993). The zonal resolution is 0.5 degrees at the equator, from where it decreases linearly towards the poles until 20°N/ S. Poleward of 20°N/ S the resolution increases gradually and is given for a specific latitude as $2 \times \cos(\text{latitude})$.

A sea ice model representing both thermodynamic and dynamic processes is coupled to the OGCM (*Fichefet and Morales*, 1997). The OGCM model is initialized with *Levitus* (1998) temperature and salinity values. The surface boundary condition is a bulk mixed layer (*Large et al.*, 1997) that is given the air temperature, air humidity, total cloudiness, surface pressure and surface windspeed (from the NCEP/NCAR reanalyses) from which surface heat fluxes are calculated. Since the NCEP reanalyses use observed SST as a lower boundary condition and observations in the South Atlantic are relatively sparse before 1958, the quality of these reanalyses could be questioned. However, *Sterl and Hazeleger* (2003) have discussed this problem in detail and came to the conclusion that using the reanalyses in the South Atlantic is reasonable.

A 200 year spin up with a restoring boundary condition on surface salinity (2 month timescale) and climatological wind and heat flux forcing has been performed (*Madec et al.*, 1998). A salinity flux correction for the 1948-1999 run has been done by applying the annual mean fluxes from the last 50 years to the interannually varying NCEP runs. Salinity variability may affect the ocean circulation due to density changes, which may then lead to pressure gradient changes and anomalous currents. Given the relatively poor quality of available freshwater flux data, this approach is necessary and is also frequently used by other modellers (e.g. POCM, *Stammer et al.*, 1996). The model output analysed in this paper consists of a 24.33 day average (i.e. 15 outputs per year) for each variable for the 1948-1999 period.

3 Data and Methods

In this study, temperature, salinity, horizontal velocities, net heat fluxes and short wave radiation are taken from the ORCA2 model output. Since the model is forced

with NCEP/ NCAR reanalyses, the data range covers the years between 1948 and 1999. The analysed region ranges from the equator to 50°S and from 70°W to 20°E. Monthly anomalies are derived by subtracting the monthly climatological mean values (52 years) from the original values. All derived anomalies are then detrended, by subtracting the linear trend from the anomalies, and smoothed with a 3 month running mean. The detrending of the data is necessary, because there is a general warming trend present in the NCEP/ NCAR reanalyses and the ORCA2 model output. The purpose of the detrending is to help isolate the natural interannual to multi-decadal signals in the timeseries under investigation, which is the main interest of this study.

Since only the net heat flux and the short wave flux fields from the ORCA2 model output were available, turbulent heat fluxes have been calculated using standard bulk formulae (see e.g. *Gill*, 1982). Sea level pressure and sea level temperature have been taken from NCEP/ NCAR reanalyses in order to calculate specific humidities. The long wave flux could only be calculated indirectly, assuming it is given as the residual between the sum of turbulent heat and short wave flux and the net heat flux. It turns out that the derived latent heat fluxes compare reasonably well with the NCEP ones in terms of magnitude and spatial extent. The sensible heat flux appears to be stronger than the NCEP flux in the subtropics to tropics. The long wave flux term appears unrealistically large. Due to the way it is calculated, it sums up the possible uncertainties of the other flux terms in the heat balance. Hence, in the following, we do not include the long wave flux in our analyses.

The average temperature and velocities of the mixed layer have been calculated by taking means from the top level to the depth of the mixed layer, which is defined as the level where the density increases by 0.01 kg m^{-3} from the surface. Geostrophic velocities have been calculated by integrating the thermal wind equations, with an assumed level of no motion at $z = -500\text{m}$. Ekman velocities have been derived using

$$\mathbf{v}_e = \mathbf{k} \times \frac{1}{\rho f z_h} \tau, \quad (1)$$

with ρ being the density, f the coriolis parameter, z_h the depth of the mixed layer

and τ the windstress vector.

Climate patterns of mixed layer temperatures, derived from the ORCA2 model output, NCEP/ NCAR SST and GISST SST (not shown) are examined using vari-max rotated empirical orthogonal functions (REOFs) (see *Preisendorfer*, 1988; *von Storch*, 1995; *Bretherton et al.*, 1992). The rotation has been performed using a minimization criteria following *Kaiser* (1958). The reason for using rotated EOFs is that they are generally less sensitive to subdomain instability, and have lower sampling errors, which occur due to closely spaced eigenvectors. Rotated EOFs maximize the variability in a certain region, and thus are more likely to reveal interpretable physical modes. The analysis has been done as follows: First, the EOFs for the variable under investigation have been calculated, their robustness has been tested using a Monte Carlo approach. The errors of the respective eigenvalues have also been investigated, using North's *Rule of Thumb* (*North et al.*, 1982). However, these tests do not influence the results of the eigenvector rotation. To test the robustness of the eigenvector rotation, we systematically increased (starting from 1) the number of rotated eigenvectors. It turns out that the first four rotated EOFs explaining the maximum amount of variance are stable and preserve their pattern and order of occurrence as long as more than five EOFs are rotated. Rotating less than five eigenvectors leads to a change in pattern for the last two modes, which is likely due to instabilities caused by *underfactoring* (*Richman*, 1986). The same robustness tests have been performed for NCEP/ NCAR reanalyses SST and GISST SST.

The REOFs are presented as homogeneous correlation maps, which are defined as the correlations between the expansion coefficients of a geophysical field and all grid points of the same field. Heterogeneous correlation maps are defined as correlations between the expansion coefficients of a field and all grid points of a different field (see also *Björnsson and Venegas*, 1997). In the following, only correlations that exceed the 95% confidence interval are discussed, unless mentioned otherwise. The confidence interval has been calculated using a standard t-test, which has been applied after reducing the degrees of freedoms for each time series, respectively (see

also *Bretherton et al.*, 1999).

The temperature tendency equation for the mixed layer temperature (see also *Seager et al.*, 2003) has been used to investigate possible forcing mechanisms. It is given as:

$$\begin{aligned} \frac{\partial T_m}{\partial t} = & - \left[\left(u_m \frac{\partial T_m}{\partial x} + v_m \frac{\partial T_m}{\partial y} \right) - \left(\frac{T_m - T_h}{h} \right) \left(u_m \frac{\partial h}{\partial x} + v_m \frac{\partial h}{\partial y} \right) \right] \\ & - \left[\left(\frac{T_m - T_h}{h} \right) \left(\frac{\partial h}{\partial t} + w_h \right) + \left(\frac{\overline{w'T'}}{h} \right)_h \right] + \frac{Q_{sfc}^{net} - Q_h^{pen}}{\rho c_p h} \end{aligned} \quad (2)$$

where T_m, u_m, v_m are the temperature and horizontal velocities vertically averaged over the depth h of the mixed layer, T_h is the temperature just below the mixed layer and w_h is the vertical velocity at the base of the mixed layer, w', T' are deviations from the mean, thus, the term describes the turbulent or Reynolds flux. Q_{sfc}^{net} is the net surface heat flux, while Q_h^{pen} is the amount of short wave radiation that penetrates through the base of the mixed layer, c_p is the specific heat capacity of ocean water, and ρ is the density of sea water. The terms in the first square brackets describe temperature changes due to horizontal processes. The terms in the second square brackets describe temperature changes due to vertical processes, that are associated with (a) mixing due to wind stirring, buoyancy loss and vertical shear ($\partial h / \partial t$), (b) vertical entrainment (w_h), and (c) turbulent mixing ($w'T'$).

The ability of the ORCA2 model to represent upper ocean temperature variability in the South Atlantic Ocean has been demonstrated by *Colberg et al.* (2004) and *Hermes and Reason* (2005). It is however necessary to check that the mixed layer depth is modelled in a realistic fashion. This is especially important in the tropics, where the east-west gradient of the thermocline is essential for equatorial dynamics. Figure 1a shows the annual mean of the thermocline depth in the tropical Atlantic, which compares reasonably well with the one shown in e.g. *Hazeleger et al.* (2002). Hence, the east-west gradient in the model appears adequate, allowing for a realistic representation of equatorial dynamics (see also *Rodgers et al.*, 2003).

The modelled net heat fluxes compare reasonably well with those from the NCEP/ NCAR reanalyses, shown in Figures 1b and 1c, in terms of magnitude and spatial distribution. However, the modelled fluxes are generally weaker in the

tropics to subtropics and near the Agulhas retroflection/ Southern Benguela, but seem to overestimate the magnitude in the area near the Angola Benguela Frontal Zone (ABFZ).

4 Oceanic variability

In the following, South Atlantic climate modes are examined using the statistical tools described above. We start off with a qualitative description of the main characteristics of the first four REOFs of mixed layer temperature, which are compared to NCEP/ NCAR reanalyses SST (*Kalnay et al.*, 1996) and UKMO GISST3.0 SST (*Rayner et al.*, 1996). We then point out the similarities and differences to previous work. Possible atmospheric linkages are investigated hereafter, followed by a detailed discussion of the forcing mechanisms associated with each mode. Note that the leading modes as discussed below are calculated for all calendar months. However, rotated EOFs were also derived for each season in order to assess the seasonality of the various modes.

It should be noted that an extension of the analysed domain into the Northern Hemisphere does not significantly alter the results presented below, as long as the northern boundary is equatorward of 10°N. A northward extension beyond that latitude leads to a subsequent pronunciation of the tropical modes, and to a reduction of the South Atlantic midlatitude modes. Since the South Atlantic is the prime target of investigation here, the domain is chosen as stated in Section 3 and is thus confined to the Southern Hemisphere.

4.1 Spatial pattern and temporal variability

The spatial pattern and corresponding expansion coefficients of the first four rotated EOFs for the mixed layer temperature (REOF(MLT)) are shown in Figure 2. The displayed modes account for 28%, 17%, 13% and 11% of the total variance, respectively. The first pattern is a southwest/ northeast oriented dipole with strongest variability concentrated in the tropical region and a connection to the west coast of

southern Africa. A wavelet analysis (not shown) of the corresponding time series of the first mode reveals strongest power on interannual time scales with a maximum amplitude in austral winter and spring.

Most of the variability of the second spatial pattern (Figure 2) is located in the subtropical region, stretching from the South African/ Namibian coast westwards to Brazil. The wavelet analysis of the corresponding time series exhibits a strong signal at the 5 year period, which is most pronounced during 1950 to 1960 and from 1970 to 1980. This mode is most pronounced in austral summer and autumn and is significantly correlated to ENSO. Maximum correlation occurs when the SOI-index leads the MLT by about one season, in agreement with *Colberg et al.* (2004) and *Sterl and Hazeleger* (2003).

The third REOF (Figure 2) displays strong variability centred in the midlatitudes between 20°W and 5°E with maximum amplitudes in austral spring. A wavelet analysis (not shown) indicates that the corresponding time series fluctuates on interannual (less than 3 years) and inter-decadal scales (10 to 40 years). Between 1948 and 1999, this mode is negative until 1960, then becomes positive until the beginning of 1980, when another negative phase starts. Also evident is a weakening of the interannual signal during 1960 to 1970.

The fourth REOF (Figure 2) shows maximum variability in the western subtropics, centred near the South Atlantic Convergence Zone (SACZ) and which ranges from interannual to decadal time scales. There is a preference for lower interannual frequencies with periods of between 5 and 8 years to occur in the first half of the analysed period, while higher frequencies with periods between 1 and 2 years are apparent thereafter. The observed mode shows strongest amplitudes in austral spring to summer, implying a possible connection with the SACZ.

The analysis is repeated with NCEP/ NCAR Reynolds reconstructed SST (*Reynolds and Smith*, 1994) and the variance explained for the modes (Figure 3) is 21%, 18%, 15% and 9%, respectively. There is a broad agreement in both spatial pattern and temporal variability between the first two modes obtained from the ORCA2 MLT and those of NCEP/ NCAR SST. The cross correlation between the time series of

the first two modes is maximum at zero lag with correlation values of 0.81 and 0.84. However, the first mode of ORCA2 MLT extends less far polewards than the NCEP/NCAR mode, and the second mode is centred farther to the east. This may be due to the higher resolution of the ORCA2 model at low latitudes.

Larger differences occur for the next two modes. Although both the NCEP/NCAR and ORCA2 modes display the major amounts of variability in the southwestern subtropics and the mid- to eastern midlatitudes, it is apparent that the order of occurrence between the modes of NCEP/NCAR SST and ORCA2 MLT is swapped. This implies that either the model or the NCEP/NCAR reanalyses may over/underestimate variability in these areas. The corresponding time series show lower correlation values with the NCEP ones (0.34 and 0.35). These values increase significantly (0.64 and 0.57) when only the second half of the 52 year time frame is considered. It has been shown by *Sterl and Hazeleger* (2003) that variability within the NCEP/NCAR reanalyses is somewhat underestimated in regions with low data coverage, e.g. the southern midlatitudes before 1980. This could explain why the modes compare better after 1980 and why the third and fourth mode are swapped. Since the model's resolution increases towards the poles, midlatitude variability may be overestimated by the model due to enhanced spatial correlation, also resulting in a different order of the modes.

The same comparison has been done with the GISST3.0 SST (not shown) and the results are found to be roughly the same. Thus, a good comparison is apparent between the first two modes, while the third and fourth modes appear to be reversed.

Differences between our modes and those of *Sterl and Hazeleger* (2003), who analyse NCEP/NCAR reanalyses SSTs, are most likely due to the applied rotation procedure used in this paper, which leads to more localized structures of variability. Thus, the first (second) mode of *Sterl and Hazeleger* (2003) shows a mixture of the first two (last two) modes shown here.

The resulting modes show larger differences with those found by *Venegas et al.* (1997), which is expected as *Venegas et al.* (1997) use a different dataset with a different grid density, do not rotate the EOFs and do not detrend the SSTs prior to

the analysis. Not detrending the data clearly favours the evolution of a monopole-like signal in the South Atlantic. Hence, the second and third mode of *Venegas et al.* (1997) show, like *Sterl and Hazeleger* (2003), a mixture of the four modes shown here.

From the comparison above, we conclude that the ORCA2 model adequately resolves the major modes of variability in the South Atlantic, and thus may be used to further investigate the relationships with the atmospheric forcing.

4.2 Atmospheric linkages - Windstress anomalies

To investigate the possible atmospheric influence on the rotated EOFs of the mixed layer temperature, windstress anomalies have been lag correlated with the expansion coefficients of the rotated EOF(MLT). The corresponding patterns are shown in Figures 4 and 5. Each sequence consists of three correlation maps, with (a) the windstress leading the MLT by 3 months, (b) zero lag between the windstress and MLT and (c) the windstress lagging the MLT by 3 months.

The pattern corresponding to the first REOF (Figures 4a to 4c) suggests positive correlations in the central to western equatorial region, peaking at zero lag. The windstress anomalies are from the west/ northwest and therefore tend to reduce the tropical trades. These wind anomalies are consistent with the observed ocean mixed layer warming (Figure 2) due to reduced vertical mixing, Ekman heat transport and reduced latent heat flux. However, the area of weaker trades does not cover the eastern tropics and the northern Benguela Current region, which are strongly affected by the warming, suggesting other processes, such as equatorial trapped waves, are responsible for the observed temperature changes there. An analysis of the mixed layer depth (not shown) reveals a deepened mixed layer in the eastern tropics, consistent with the observed warming. In the western tropics, the mixed layer depth tends to be shallower than average, since the southeasterly trades are reduced implying a reduced accumulation of warm water to the west.

The lagged correlation analysis between the windstress anomalies and the second mode (Figures 4d to 4f) reveals highest correlations in the subtropics, where the

windstress anomalies tend to reduce the trades. The correlations are strongest one season before and at zero lag, suggesting that ocean temperatures are mainly driven by wind induced changes in latent heat flux. This assumption is further supported by the mixed layer depth (not shown) which is generally decreased over the regions of strongest warming, suggesting a stronger vertical stratification due to reduced wind stirring and increased heat flux into the ocean. The mechanisms altering the mixed layer depth for this mode are thus different from those of the first mode and will be further discussed in the next section.

The correlations between the windstress anomalies and the third REOF(MLT), shown in Figures 5a to 5c, are much smaller compared to the other two modes, suggesting that the windstress is less important in driving upper ocean temperatures there. Strongest correlations occur in the midlatitudes at zero lag. The windstress acts to reduce the prevailing westerlies there and supports ocean warming due to reduced vertical mixing, wind driven Ekman heat transport and reduced latent heat flux.

Relatively weak correlations between the windstress anomalies and the fourth REOF(MLT) (Figures 5d to 5f) are apparent. The anomalous windstress tends to enhance the subtropical anticyclone for warm phases of this mode, thereby suggesting that enhanced wind stirring and increased turbulent heat fluxes may act to dampen the observed MLTs.

4.3 Forcing fields

To further investigate the forcing mechanisms behind the four modes, lagged field-index regressions, using least squares, have been performed between all terms arising in the temperature tendency equation (2) and the expansion coefficients (the lagged regression analyses allow for a direct comparison of the forcing terms). Typical values for the four modes are calculated by taking averages over positive and negative values of the resulting regression fields respectively.

A significant region is defined as that area for which the cross correlation between the REOFs and the mixed layer temperature anomalies exceeds the 95% confidence

interval (Figure 2). The bar diagrams for each REOF are displayed in Figure 6. The numbers 1 to 7 indicate the different forcing terms in equation (2). Positive (negative) values indicate a forcing term that acts to enhance (reduce) the temperature tendency and therefore favours mixed layer warming (cooling).

In the following, we present sequences of heterogeneous correlation maps between the dominant forcing terms and the expansion coefficients. Each sequence consists of three correlation maps, with (a) the forcing field leading the MLT by 3 months, (b) zero lag between the forcing field and MLT (c) the forcing field lagging the MLT by 3 months.

First REOF(MLT)

According to Figure 6a, the dominant forcing term for the first REOF is vertical entrainment. It is positively correlated with the time series of the first REOF(MLT) in the central and eastern tropics (see Figures 7a to 7c), with maximum correlation at zero lag (Figure 7b). Since vertical entrainment only acts to cool the mixed layer, as colder water is entrained from deeper ocean levels, positive correlation imply reduced mixing from the subsurface ocean into the mixed layer, which favours ocean warming. The annual cycle of the vertical entrainment term (not shown) reveals enhanced entrainment during the austral summer months, consistent with the annual cooling. Therefore, reduced entrainment is plausible in explaining the observed warming.

Net surface heat flux (Figure 7d to 7f), is the second largest term in magnitude (Figure 6a), and is negatively correlated with the first REOF(MLT) in the central to eastern tropical region. The negative correlation suggests that net surface heat flux acts to dampen the prevailing upper ocean temperature anomalies. The net heat flux term reaches strongest negative correlations 3 months after the maximum upper ocean temperature anomalies occur, indicating that increased turbulent heat fluxes due to the observed upper ocean warming may become important in the heat flux balance and thereby weaken the anomalous ocean temperatures. The correlation sequence for the latent heat flux (Figures 7g to 7i) confirms this assumption as strong negative correlations in the central to eastern tropical Atlantic are evident.

The pattern of the net surface heat flux and latent heat flux match reasonably well. However, the net surface heat flux is stronger near the equator, whereas the latent heat flux shows is stronger further southeast. The differences between the net surface and the latent heat flux may be due to the way the latter has been calculated, which involved some filtering and interpolation in order to match NCEP/NCAR fields with ORCA2 fields. Positive correlations between the surface heat flux and the first REOF(MLT) are evident in the western tropics between 40°W and 30°W , suggesting that surface heat fluxes contribute to the warming there. These correlations are strongest a season before the largest temperature anomalies.

The correlation sequence for the turbulent mixing (not shown) reveals strongest positive correlations near the equator at zero lag, favouring warming there. Cooling is supported southward of that, due to increased mixing. The horizontal advection sequence (Figures 8a to 8c) suggests warming over most of the tropical Atlantic region, with the exception of the central to eastern tropics (15°W - 15°E and 0 - 4°S), which is the region where vertical entrainment dominates. Highest correlation is found in the western tropics, peaking at zero lag (Figure 8b). The underlying anomalous oceanic currents, shown in Figures 8d to 8f, act to reduce the South Equatorial Current and the North Brazil Current. Hence, these current anomalies imply a reduced transport of cool water towards to the western tropics, favouring the observed warming there.

Second REOF(MLT)

Net surface heat flux is the dominant forcing term for the second REOF (Figure 6b), which reflects ENSO. The corresponding correlation sequence is shown in Figures 9a to 9c. The correlation is positive in the subtropics with greatest values at 3 months lead and at zero lag (Figures 9a and 9b, respectively). The regression and correlation analysis has been repeated with the different terms of the heat balance (not shown). The results suggest that the latent heat flux is the dominant term in the net surface flux, in agreement with *Sterl and Hazeleger (2003)* and *Colberg et al. (2004)*. The correlation sequence for latent heat flux resembles the one for the total heat flux (Figure 9a to 9c). Therefore, changes in temperatures are likely to

be caused by changes in evaporation driven by anomalous winds (Figure 4d to 4f). The turbulent mixing, and vertical entrainment terms of Equation 2 also contribute towards the observed warming, since the trades are weakened. However, the first mixing term ($-\frac{\Delta T}{h} \frac{\partial h}{\partial t}$) in this case implies ocean cooling, due to increased heat loss associated with the shallower mixed layer.

Third REOF(MLT)

The significant forcing terms for the third mode are horizontal advection, the first mixing term ($-\frac{\Delta T}{h} \frac{\partial h}{\partial t}$) and the surface heat flux term (Figure 6c). The correlation sequence for the horizontal advection is shown in Figures 10a to 10c. The positive areas in the central to eastern midlatitudes match well with the observed warming shown in Figure 2. Two centres of strong correlations occur at around 20°W, 40-50°S and between 0° and 10°E, 40-50°S. They are strongest at 3 month lead and at zero lag (Figures 10a and 10b). The underlying anomalous ocean currents, shown in Figures 10d to 10f, show strongest correlations in the midlatitudes near 20°W, where they are mainly southward, suggesting a reduced northward Ekman transport of cold water into the area, thus contributing to the observed warming there (the mean westerly winds drive a northward Ekman transport in the midlatitudes). The same is also true to some extent for the region near 0°E.

Splitting the velocities into a geostrophic and an Ekman part (both not shown), indicates that the area between 10°W and 20°E is dominated by anomalous southward Ekman flow, consistent with the windstress anomalies discussed in Section 4.2 (Figures 5a to 5c). Hence, warming there is likely due to a reduced northward meridional Ekman transport of cold water, implying reduced upper ocean cooling from high latitudes. The area west of 15°W shows high correlation coefficients with the geostrophic velocities. Also evident are increased correlation values in the far western midlatitudes, implying that changes in the opposing Falklands/ Malvinas and Brazil Currents may be important in driving upper ocean temperatures there. However, although the correlation coefficients are much higher compared to the ones seen for the Ekman velocities, they are just below the 95% confidence interval. This result suggests that two different mechanisms associated with two different time

scales (and certainly different degrees of freedom) are present here.

This possibility is further investigated by taking the means over the regions of highest correlations of meridional geostrophic (10-20°W, 40-50°S) and Ekman velocities (0-10°E, 40-50°S), respectively. These means are correlated with the third expansion coefficient of the REOF(MLT). The correlations and their corresponding wavelet pattern are shown in Figure 11. The wavelet pattern associated with the geostrophic velocity has a peak at a period between 10 and 20 years, it is related to the inter-decadal variability described in the first section. This peak is also present in the Ekman related pattern. Furthermore, the Ekman related pattern possesses another peak at the 5 year period and shows significant correlations with ENSO ($r = 0.34$). This result is in agreement with *Colberg et al.* (2004) who showed that, during ENSO, significant temperature changes in the South Atlantic Ocean are due to changes in the subtropical high pressure system, that in turn drive anomalous Ekman heat transport in this region.

The western midlatitudes are characterized by inter-decadal variability that is related to changes in the geostrophic currents (significant at 90% but not 95% confidence interval). Due to the shortness of the available data, it is not clear whether the inter-decadal variability describes a real physical mode or not. However, the timing, region of variability, and the baroclinic nature of this mode are similar to that found by *Reason* (2000) and *Wainer and Venegas* (2001).

The second largest term is the first mixing term ($-\frac{\Delta T}{h} \frac{\partial h}{\partial t}$, sequence not shown). It is positively correlated over areas of observed upper ocean warming, suggesting that the weakened westerlies (Figure 5) between 20°W-20°E and 40-50°S lead to reduced vertical mixing processes, thereby favouring the observed upper ocean warming. The associated mixed layer depth shows significant and positive correlation values in a small area between 18°W-20°E and 40-45°S, implying a deepened mixed layer there. This result is counter-intuitive to the above finding of reduced westerlies in the area, which imply a shallower mixed layer depth, suggesting that the mechanisms responsible for altering the mixed layer depth are not related to the apparent windstress anomalies. This assumption is supported by the fact that the

correlation sequence for the mixed layer depth in the region of significant correlations reveals a strong oscillation on inter-decadal time scales, similar to what has been discussed above for the geostrophic velocities. It is possible that changes in geostrophic advection and associated divergence may thus contribute towards the anomalous mixed layer deepening in this region.

The calculated positive and negative mean values (Figure 6) for the net surface heat flux are of the same magnitude for this mode. The strongest negative (positive) correlations occur over regions of strong ocean warming (cooling) one season after the temperature anomalies peak, suggesting that the net heat flux into the ocean is reduced (enhanced) due to changes in the turbulent heat fluxes. Hence, the net surface heat flux damps the temperature anomalies, similar to what has been discussed for the first mode.

Fourth REOF(MLT)

The bar diagram (Figure 6d) for the last REOF of the mixed layer temperature suggests that the net heat flux term is the most important term in creating the anomalous temperatures. Its sequence is shown in Figures 12a to 12c. This term shows maximum correlation in the western/ central subtropics at one season lead and at zero lag. The regression and correlation analyses have been repeated with the turbulent heat and short wave flux terms. It turns out that the latent and sensible heat fluxes are negatively correlated over the region of warm temperature anomalies, counteracting the observed warming in response to the stronger South Atlantic Anticyclone (Figures 5d to 5f). Warming on the other hand is favoured by anomalous short wave flux (not shown), between 20-30°S and 10-30°W. The change in insolation partly covers the region of anomalous MLT, but counteracts the observed temperatures elsewhere. Reduced short wave flux also suggests enhanced cloud cover and thus decreased emitted long wave radiation. Since the MLT anomaly is centred near the SACZ (see also *Robertson and Mechoso, 2000*), a region associated with convection and strong cloud cover, changes in insolation are likely to be important and substantially affect upper ocean temperatures here.

The first vertical mixing term ($-\frac{\Delta T}{h} \frac{\partial h}{\partial t}$, Figures 12d to 12f) counteracts the

temperature anomalies and shows strongest correlations at zero and at 3 month lag. The enhanced windstress leads to mixed layer cooling as more cold water is entrained.

The corresponding correlation with the advection term in Figure 6d indicates (not shown) relatively strong negative correlation stretching northwestward across the South Atlantic basin from 20°E to the Brazil coast implying an enhanced Benguela Ocean and South Equatorial Current and thus advect more cool water into the area of maximum upper ocean warming associated with this mode.

4.4 Heat and Volume Transport at 30°S

We have examined changes in heat and volume transport associated with each mode but only discuss the second leading mode because this one appears to be most obviously contributed to by changes of the subtropical gyre. We focus on the meridional component of the heat and volume transport and define an east-west section that lies within the area of highest variability displayed by this mode. As before, we use correlation analyses to investigate possible linkages between the REOF and the transports. Heat and volume transports are derived using (a) total model velocities, and (b) geostrophic model velocities.

The east-west section of correlation between the second REOF(MLT) and the heat transport anomalies through 30°S is shown in Figures 13a to 13c. Three regions of significant correlation are apparent. Region 1 is located in the upper ocean to a depth of about 30m, stretching from 30°W to 0°. The correlation is positive and indicates an enhanced northward or reduced southward heat transport, during phases of positive MLT anomalies. Region 2 shows negative correlation and is significant at depths of 50m to 200m, and is centred between 0°E to 10°E. The negative correlation thus indicates a reduced northward or enhanced southward heat transport. Region 3 is smaller than the other two. Significant positive correlation is centred at $z = 25m$ near 15°E, thus indicating enhanced northward or reduced southward heat transport there.

To further investigate the nature of the anomalous transports, we calculate

anomalies corresponding to (a) transport of temperature due to anomalous volume transport, (i.e. $v'T$) and (b) advection of anomalous temperature by the mean volume transport (i.e. vT'). It turns out that the positive and negative anomalies of Region 1 and 2 are mainly due to anomalous volume transport, whereas the positive anomaly apparent in Region 3 is related to the vT' term.

The vertical section resulting from the correlation analyses including only geostrophic velocities is shown in Figures 13d to 13f. The negative anomaly between 0-10°E, apparent from the surface to about 200m depth (Region 2), resembles the one seen in Figures 13a to 13c and we thus may conclude that the anomalous heat transport there is mainly due to anomalous geostrophic currents. The eastern located positive anomaly near 15°E in Figures 13a to 13c (Region 3) does not appear in Figures 13d to 13f, but becomes apparent when calculating the heat transport due to anomalous temperatures (i.e. vT') (not shown). Furthermore, the western positive anomaly near 0-30°W in Figures 13a to 13c (Region 1), does not appear at all in any of the geostrophic related correlation analyses, therefore indicating indirectly that it may be related to anomalous meridional Ekman heat transports. This suggestion is further supported since the correlation analyses between the second REOF and meridional Ekman heat transport anomalies (Figure 14a to 14c) are positive in an area stretching from the Benguela Current region northwestwards along the South Equatorial Current, therefore matching with the area seen in the vertical section of Figures 13a to 13c. Thus, the analyses above suggest that changes in the heat transport associated with the second mode are mostly induced via changes in volume transport, which are related to anomalous currents. The Benguela Ocean Current is reduced (enhanced) at 30°S during positive (negative) phases of the second REOF, and thus transports less (more) cold water northwards, which subsequently leads to warming (cooling) in the significant region of the second REOF shown within the bold lines in Figure 2. The induced anomalous heat transport is primarily caused by anomalous geostrophic currents and reaches depths of 200m. On the other hand, anomalous Ekman meridional heat transport dominates the region west of 0°W (Region 1) and is confined to the upper 50m.

The analyses therefore suggest that the second mode is associated with gyre modifications, leading to anomalous volume fluxes and thus anomalous heat fluxes at the eastern margin of the subtropical gyre. A possible wind induced mechanism could explain this as follows. The reduced windstress (Figures 4d to 4f) associated with positive phases of the second REOF(MLT) leads to a reduction of the southwestward directed Ekman volume transport. This in turn affects the sea surface height in the centre of the subtropical gyre and thus weakens the outward directed pressure gradient, thereby weakening the geostrophic balanced gyre circulation. We would therefore expect changes in the sea surface height to be associated with this mode. Correlation analyses between the second REOF and sea surface height anomalies (Figure 14d to 14f) indeed suggest a reduced sea surface height during positive phases of this mode, thereby supporting this idea. However, correlation values are above the 90% but below the 95% confidence interval.

5 Summary and conclusions

In this work, the variability of the South Atlantic Ocean has been examined by means of a global OGCM (ORCA2) forced with 52 years of NCEP reanalyses. A rotated EOF analysis of MLT has been applied and the four leading modes have been investigated. They appear to divide the South Atlantic into four subdomains, each with typical time and spatial scales. These modes are (a) the tropical mode, with primarily interannual variability mainly located in the tropics and northern Benguela, (b) the northwestern-southeastern orientated mode, with variability between interannual and inter-decadal time scales, (c) the midlatitude mode with variability on both interannual and inter-decadal time scales, forming an east-west oriented dipole in the midlatitudes and (d) the southwestern subtropical/ midlatitude mode, that fluctuates on an interannual and inter-decadal time scale. Correlation analyses between these modes and windstress suggests that all modes are primarily driven by the atmospheric circulation.

The mechanisms that create the anomalous temperatures are different for each

mode. The first mode is connected to anomalous northeasterly windstresses that reduce the prevailing trades in the central to western tropics. Hence, surface latent heat fluxes are reduced, leading to warming there. Furthermore, these anomalous winds tend to reduce the zonal component of the southwestward directed upper ocean mean currents. Thus, less cold water is transported towards the western tropics, favouring warming there.

The windstress anomalies do not favour warming over the eastern tropics and northern Benguela region, suggesting non-local atmospheric influences such as equatorial Kelvin wave propagation may be responsible for creating these temperature anomalies (as suggested by *Carton and Huang*, 1994; *Florenchie et al.*, 2003, 2004). For example, the reduced trades over the western tropics (Figure 4) imply relative Ekman convergence near the equator and the generation of downwelling which thus may trigger Kelvin waves that lead to warming to the east a month or two later. In fact, the strongest warming associated with this mode occurs during 1963, which was a 'Benguela-Niño' year (*Shannon et al.*, 1986), suggesting a possible connection between this mode and these events. However, although other strong warm events such as the one in 1984 are captured by the time series of this mode, they are not as extreme as the one in 1963. The analysis (Figures 6 and 7) suggests that warming in the central to eastern tropics is connected to reduced upwelling mainly due to reduced vertical entrainment and, to lesser extent, reduced turbulent mixing. The mode analysed in this paper shows strong similarities with the Atlantic Zonal Gradient Mode (also Equatorial Mode), described by *Zebiak* (1993); *Enfield and Mayer* (1997); *Carton et al.* (1996); *Ruiz-Barradas et al.* (2000).

The second mode is connected to reduced trade winds over the subtropics. These lead to changes in the latent heat flux, that in turn alter upper ocean temperatures. Changes in horizontal advection and vertical mixing processes make smaller contributions to the observed ocean temperature changes. The timing and spatial structure of this mode suggests a connection to ENSO, which is in agreement with *Reason et al.* (2000), *Sterl and Hazeleger* (2003) and *Colberg et al.* (2004). In addition, it is found that trade wind modulations significantly alter the Ekman related meridional

volume and heat transport, which in turn lead to changes in the gyre circulation and thus geostrophic related volume and heat transports. These anomalous transports are strongest in the Benguela ocean current region and reach depths of up to 200m.

For the third mode, the midlatitude westerlies are weakened and result in a reduced northward directed Ekman heat transport, which leads to warming in the central to eastern midlatitudes. However, on inter-decadal scales, there are changes in the geostrophic currents that alter the northward (southward) flowing Falklands/Malvinas (Brazil) Current, bringing cooler (warmer) water into the area. This mode may be connected to the inter-decadal SST signal found by *Wainer and Venegas* (2001).

Upper ocean temperature anomalies for the fourth mode respond to changes in the net heat flux into the ocean, which is increased (reduced) during warm (cold) phases. Associated with this mode are changes in the strength of the South Atlantic Anticyclone, which mainly acts to enhance (reduce) entrainment into the mixed layer during positive (negative) phases and thus dissipates the observed temperature anomalies.

The results of this study suggest that the ORCA2 model output can be usefully applied to diagnose the major modes of South Atlantic variability and the mechanisms associated with them. The advantage of the model output becomes most apparent when examining the meridional heat transport associated with the second leading mode and in the analyses of the midlatitude mode, where advection of heat is partly due to the baroclinic structure of the ocean, and cannot be diagnosed from surface based data sets. The results also emphasize the importance and dependence on the choice of statistical tools used to diagnose the leading modes. The rotated EOF analysis results in more localized structures of the analysed fields, and as a consequence, the tropical and subtropical modes are clearly separated from each other.

There are implications for both regional and global scales suggested by this study, e.g., the second leading mode is associated with anomalous heat and volume transports and gyre modifications, which in turn may affect the global heat balance

and thus the thermohaline circulation. This study provides evidence that upper ocean temperature anomalies in coastal regions, e.g., the Benguela, are strongly affected by the large scale modes, implying variability on interannual to decadal time scales there which has implications for understanding of the occurrences of extreme warm/ cool events in this region. The Benguela upwelling system contains one of the richest regional fisheries in the world and supports a high marine biodiversity, thus better understanding of its variability and its sensitivity to large scales modes is a high priority.

6 Acknowledgements

We should like to thank the three anonymous reviewers for their thorough and constructive comments, which helped to improve the document. Financial support from the Benguela Current Large Marine Ecosystem (BCLME) is gratefully acknowledged.

References

- Björnsson, H., and S. A. Venegas (1997), *A manual for EOF and SVD Analyses of Climatic Data*, Centre for Climate and Global Change Research, McGill University.
- Blanke, B., and P. Delecluse (1993), Variability of the Tropical Atlantic Ocean simulated by a general circulation model with two different mixed layer physics, *J. Phys. Oceanogr.*, *23*, 1363–1388.
- Bretherton, C. S., C. Smith, and J. M. Wallace (1992), An intercomparison of methods for finding coupled patterns in climate data, *J. Clim.*, *5*, 354–369.
- Bretherton, C. S., M. Widman, V. P. Dymnikov, J. M. Wallace, and I. Blade (1999), The effective number of spatial degrees of freedom of a time-varying field, *J. Clim.*, *12*, 1990–2009.
- Carton, J. A., and B. Huang (1994), Warm events in the Tropical Atlantic, *J. Phys. Oceanogr.*, *24*, 888–903.
- Carton, J. A., X. Cao, B. S. Giese, and A. M. da Silva (1996), Decadal and inter-annual SST variability in the Tropical Atlantic Ocean, *J. Phys. Oceanogr.*, *26*, 1165–1175.
- Colberg, F., C. J. C. Reason, and K. Rodgers (2004), South Atlantic Response to El Niño-Southern Oscillation induced Climate Variability in an OGCM, *J. Geophys. Res.*, *109*, C12015, doi:10.1029/2004JC002301.
- Enfield, D. B., and D. A. Mayer (1997), Tropical Atlantic SST variability and its relation to El Niño-Southern Oscillation, *J. Geophys. Res.*, *102*, 929–945.
- Fichefet, T., and M. A. Morales (1997), Sensitivity of a global sea ice model to the treatment of ice thermodynamics and dynamics, *J. Geophys. Res.*, *91*, 5037–5046.

- Florenchie, P., J. R. E. Lutjeharms, C. J. C. Reason, S. Masson, and M. Rouault (2003), The source of the Benguela Niños in the South Atlantic Ocean, *Geophys. Res. Lett.*, *30*(10), 1505, doi:10.1029/2003GLO17172.
- Florenchie, P., C. J. C. Reason, J. R. E. Lutjeharms, M. Rouault, and C. Roy (2004), Evolution of interannual warm and cold events in the south-east Atlantic Ocean, *J. Clim.*, *17*, 2318–2334.
- Gent, P. R., and J. C. McWilliams (1990), Isopycnal mixing in ocean circulation models, *J. Phys. Oceanogr.*, *20*, 150–156.
- Gill, A. E. (1982), *Atmosphere-Ocean Dynamics, International Geophysics Series*, vol. 30, Academic Press.
- Gordon, A. L. (1986), Inter-Ocean exchange of thermocline water, *J. Geophys. Res.*, *91*, 5037–5046.
- Haarsma, R. J., E. J. D. Campos, W. Hazeleger, C. Severijns, A. R. Piola, and F. Molteni (2005), Dominant modes of variability in the South Atlantic: A study with a hierarchy of ocean-atmosphere models, *J. Clim.*, *18*, 1719–1735.
- Hazeleger, W., P. de Vries, and Y. Friocourt (2002), Sources of the Equatorial Undercurrent in the Atlantic in a High-Resolution Ocean Model, *J. Phys. Oceanogr.*, *33*, 677–693.
- Hermes, J. C., and C. J. C. Reason (2005), Ocean Model Diagnosis of Interannual Coevolving SST Variability in the South Indian and South Atlantic Ocean, *J. Clim.*, *18*, 2864–2882.
- Kaiser, H. F. (1958), The varimax criterion for analytic rotation in factor analysis, *Psychometrika*, *23*, 187–200.
- Kalnay, E., et al. (1996), The NCEP/NCAR, 40-Year Reanalysis Project, *Bull. Am. Meteorol. Soc.*, *77*(3), 437–471.

- Large, G. L., G. Danabasolgu, and S. C. Doney (1997), Sensitivity to Surface Forcing and Boundary Layer Mixing in a Global Ocean Model: Annual-Mean Climatology, *J. Phys. Oceanogr.*, *27*, 2418–2447.
- Levitus, S. (1998), World Ocean Atlas 1998, *Tech. rep.*, US Department of Commerce.
- Madec, G., P. Delecluse, M. Imbard, and C. Levy (1998), OPA 8.1 Ocean General Circulation Model reference manual, *Institut Pierre Simon Laplace*, *11*, 91.
- North, G. R., T. L. Bell, R. F. Cahalan, and F. J. Moeng (1982), Sampling errors in the estimation of empirical orthogonal functions, *Mon. Wea. Rev.*, *110*, 699–706.
- Palastanga, V., C. S. Vera, and A. R. Piola (2002), On the leading modes of sea surface temperature variability on the South Atlantic ocean, *CLIVAR Exchanges*, *7*(3-4), 12–15.
- Palastanga, V., C. S. Vera, and A. R. Piola (2005), South Atlantic Sea surface temperature variability from seasonal to interdecadal time scales, *Submitted*.
- Preisendorfer, R. W. (1988), *Principal Component Analyses in Meteorology and Oceanography*, 425 pp., Elsevier, Amsterdam.
- Rayner, N. A., E. B. Horton, D. E. Parker, C. K. Folland, and R. B. Hackett (1996), Version 3.0 of the Global Sea-Ice and Sea Surface Temperature Data Set, *UK Met. Office, Bracknett*, clim. Res. Tech. Note. 74.
- Reason, C. J. C. (2000), Multidecadal climate variability in the subtropics/ mid-latitudes of the southern hemisphere oceans, *Tellus*, *52A*, 203–223.
- Reason, C. J. C., and D. Jagadheesha (2005), Relationships between South Atlantic SST Variability and Atmospheric Circulation over the South African Region during Austral Winter, *J. Clim.*, *18*, 3339–3355.

- Reason, C. J. C., R. J. Allan, J. A. Lindesay, and T. J. Ansell (2000), ENSO and climatic signals across the Indian Ocean basin in the global context: Part I, interannual composite patterns, *Int. J. Climatol.*, *20*, 1285–1327.
- Reason, C. J. C., M. Rouault, J. L. Melice, and D. Jagadheesha (2002), Winter rainfall variability in SW South Africa and large scale-ocean-atmosphere interactions, *Meteorol. Atm. Phys.*, *80*(1-4), 19–29.
- Reynolds, R. W., and T. M. Smith (1994), Improved global sea surface temperature analyses using optimum interpolation, *J. Clim.*, *7*, 929–948.
- Richman, M. B. (1986), Rotation of Principal Components, *J. Climatol.*, *6*, 293.335.
- Robertson, A. W., and C. R. Mechoso (2000), Interannual and Interdecadal Variability of the South Atlantic Convergence Zone, *Mon. Wea. Rev.*, *128*, 2947–2957.
- Robertson, A. W., J. D. Farrara, and C. R. Mechoso (2003), Simulations of the Atmospheric Response to South Atlantic Sea Surface Temperature Anomalies, *J. Clim.*, *16*, 2540–2551.
- Rodgers, K. B., B. Blanke, G. Madec, O. Aumont, P. Ciais, and J. C. Dutay (2003), Extratropical Sources of Equatorial Pacific Upwelling in an OGCM, *Geophys. Res. Lett.*, *30*(2), 1084, doi:10.1029/2002GL016003.
- Rouault, M., P. Florenchie, N. Fauchereau, and C. J. C. Reason (2003), South East tropical Atlantic warm events and southern African rainfall, *Geophys. Res. Lett.*, *30*(5), 8009, doi:10.1029/2002GLO14840.
- Ruiz-Barradas, A., J. A. Carton, and S. Nigam (2000), Structure of interannual to decadal climate variability in the tropical Atlantic sector, *J. Clim.*, *13*, 3285–3297.
- Schmitz, W. J. (1995), On the interbasin scale thermohaline circulation, *Rev. Geophys.*, *33*, 151–173.

- Seager, R., R. Murtugudde, N. Naik, A. Clement, N. Gordon, and J. Miller (2003), Air-sea interaction and the seasonal cycle of the subtropical anticyclones, *J. Clim.*, *16*, 1948–1966.
- Shannon, L. V., A. J. Boyd, G. Brundrit, and J. Taunton-Clark (1986), On the existence of an El Niño type phenomenon in the Benguela system, *J. Mar. Res.*, *44*, 495–520.
- Smith, W. H. F., and D. T. Sandwell (1997), Global Sea Floor Topography from Satellite Altimetry and Ship Depth Soundings, *Science*, *277*(5334), 1956–1962.
- Stammer, D., R. Tokmakian, A. Semtner, and C. Wunsch (1996), How well does a $1/4^\circ$ global circulation model simulate large-scale oceanic observations ?, *J. Geophys. Res.*, *101*(10), 25,779–25,811.
- Sterl, A., and W. Hazeleger (2003), Coupled variability and air-sea interaction in the South Atlantic Ocean, *Climate Dyn.*, *21*, 559–571.
- Venegas, S. A., L. A. Mysak, and D. N. Straub (1996), Evidence for interannual and interdecadal climate variability in the South Atlantic, *Geophys. Res. Lett.*, *23*(19), 2673–2676.
- Venegas, S. A., L. A. Mysak, and D. N. Straub (1997), Atmosphere-ocean coupled variability in the South Atlantic, *J. Clim.*, *10*, 2904–2920.
- Venegas, S. A., L. A. Mysak, and D. N. Straub (1998), An interdecadal climate cycle in the South Atlantic and its links to other ocean basins, *J. Geophys. Res.*, *103*(C11), 24,723–24,736.
- von Storch, H. (1995), *Analysis of Climate Variability: Application of Statistical Techniques*, chap. Spatial patterns: EOFs and CCA, pp. 227–257, Springer Verlag.
- Wainer, I., and S. A. Venegas (2001), South Atlantic Multidecadal Variability in the Climate System Model, *J. Clim.*, *15*, 1408–1420.

Zebiak, S. E. (1993), Air-sea interaction in the equatorial atlantic region, *J. Clim.*,
6, 1567–1580.

List of Figures

- Figure 1** Annual mean of (a) ORCA2 thermocline depth, (b) the net heat flux as modelled by ORCA2 and (c) the net heat flux from NCEP/ NCAR reanalyses. Positive (negative) contour lines are solid (dashed), zero contour line is omitted, the contour interval is 10 [m] for (a) and 20 [Wm^{-2}] for (b) and (c). 34
- Figure 2** From top to bottom: First four rotated EOFs of ORCA2 MLT, left: Spatial pattern as homogeneous correlation maps, positive (negative) contour lines are solid (dashed), zero contour line is dashed - dotted, the contour interval is 0.2, right: Corresponding time series normalized by their standard deviation. The raw time series is shown in black. The thick grey line represent the time series smoothed with a one year running mean. Significant regions (95% significance interval) are within the thick line in the spatial plot. 35
- Figure 3** From top to bottom: First four rotated EOFs of NCEP/ NCAR SST. Left: Spatial pattern as homogeneous correlation maps, positive (negative) contour lines are solid (dashed), zero contour line is dashed - dotted, the contour interval is 0.2. Right: Corresponding time series normalized by their standard deviation. The raw time series is shown in black. The thick grey line represent the time series smoothed with a one year running mean. Significant regions (95% confidence interval) are within the thick line in the spatial plot. 36
- Figure 4** Sequences of lagged correlation between windstress and the first two REOF(MLT). Upper panel: *lead* = 3*months*, middle panel: *lag* = 0, and lower panel *lag* = 3*months*. Lead means REOF(MLT) leads the forcing field and lag means REOF(MLT) lags the forcing field. 37

Figure 5 Sequence of lagged correlation between windstress and the third and fourth REOF(MLT). Upper panel: $lead = 3months$, middle panel: $lag = 0$, and lower panel: $lag = 3months$. Lead means REOF(MLT) leads the forcing field and lag means REOF(MLT) lags the forcing field. 38

Figure 6 Bar diagram of the lagged regression analyses between the forcing terms in the temperature tendency equation (2) and the first four REOF(MLT). Bars correspond from left to right: (1) $-\mathbf{v} \cdot \nabla T$, (2) $\frac{\Delta T}{h} \mathbf{v} \cdot \nabla h$, (3) $-\frac{\Delta T}{h} w_h$, (4) $-\frac{\Delta T}{h} \frac{\partial h}{\partial t}$, (5) $-\frac{\overline{w'T'}}{h}$, and (6) $\frac{Q_{sfc}^{net}}{\rho c_p h}$. See text for details. . . . 39

Figure 7 Sequence of the lagged correlation between the first REOF(MLT) and $-\frac{\Delta T}{h} w_h$, (left), Q_{sfc}^{net} (middle) and latent heat flux (right). Upper panel: $lead = 3months$, middle panel: $lag = 0$, and lower panel: $lag = 3months$. Lead means REOF(MLT) leads the forcing field and lag means REOF(MLT) lags the forcing field. Positive (negative) contour lines are solid (dashed). The zero contour line is dashed - dotted. The contour interval is 0.2. 40

Figure 8 Sequence of the lagged correlation between the first REOF(MLT) and $-\mathbf{v} \cdot \nabla T$ (left) and \mathbf{v} (right). Upper panel: $lead = 3months$, middle panel: $lag = 0$, and lower panel: $lag = 3months$. Lead means REOF(MLT) leads the forcing field and lag means REOF(MLT) lags the forcing field. Positive (negative) contour lines are solid (dashed). The zero contour line is omitted. The contour interval is 0.2. 41

Figure 9 Sequence of the lagged correlation between the second REOF(MLT) and $\frac{Q_{sfc}^{net}}{\rho c_p h}$. Upper panel $lead = 3months$, middle panel: $lag = 0$, and lower panel: $lag = 3months$. Lead means REOF(MLT) leads the forcing field and lag means REOF(MLT) lags the forcing field. Positive (negative) contour lines are solid (dashed). The zero contour line is omitted. The contour interval is 0.2. 42

Figure 10 Sequence of the lagged correlation between the third REOF(MLT) and $-\mathbf{v} \cdot \nabla T$, and \mathbf{v} . Upper panel: *lead* = 3*months*, middle panel: *lag* = 0, and lower panel: *lag* = 3*months*. Lead means REOF(MLT) leads the forcing field and lag means REOF(MLT) lags the forcing field. Positive (negative) contour lines are solid (dashed). The zero contour line is omitted. The contour interval is 0.2. 43

Figure 11 (a) Wavelet plot (upper) of the lagged correlation sequence (lower) between the third REOF(MLT) and meridional geostrophic velocities averaged over the region 10-20°W and 40-50°S, (b) as for (a) but for meridional Ekman velocities averaged over the region 0-10°E and 40-50°S. 44

Figure 12 Sequence of the lagged correlation between the fourth REOF(MLT) and Q_{sfc}^{net} , and $-\frac{\Delta T}{h} \frac{\partial h}{\partial t}$. Upper panel: *lead* = 3*months*, middle panel: *lag* = 0 and lower panel *lag* = 3*months*. Lead means REOF(MLT) leads the forcing field and lag means REOF(MLT) lags the forcing field. Positive (negative) contour lines are solid (dashed). The zero contour line is omitted. The contour interval is 0.2. 45

Figure 13 Sequence of vertical section of correlation between the second REOF(MLT) and heat transport anomalies through 30°S. The transport has been calculated using total model velocities (left) and geostrophic velocities (right). Upper panel: *lead* = 3*months*, middle panel: *lag* = 0, and lower panel: *lag* = 3*months*. Lead means REOF(MLT) leads the forcing field and lag means REOF(MLT) lags the forcing field. Positive (negative) contour lines are solid (dashed). The zero contour line is omitted. The contour interval is 0.1. 46

Figure 14 Sequence of the lagged correlation between the second REOF(MLT) and the meridional Ekman heat transport (left) and SSH anomaly (right). Upper panel: *lead* = 3*months*, middle panel: *lag* = 0, and lower panel: *lag* = 3*months*. Lead means REOF(MLT) leads the forcing field and lag means REOF(MLT) lags the forcing field. Positive (negative) contour lines are solid (dashed). The zero contour line is omitted. The contour interval is 0.1. 47

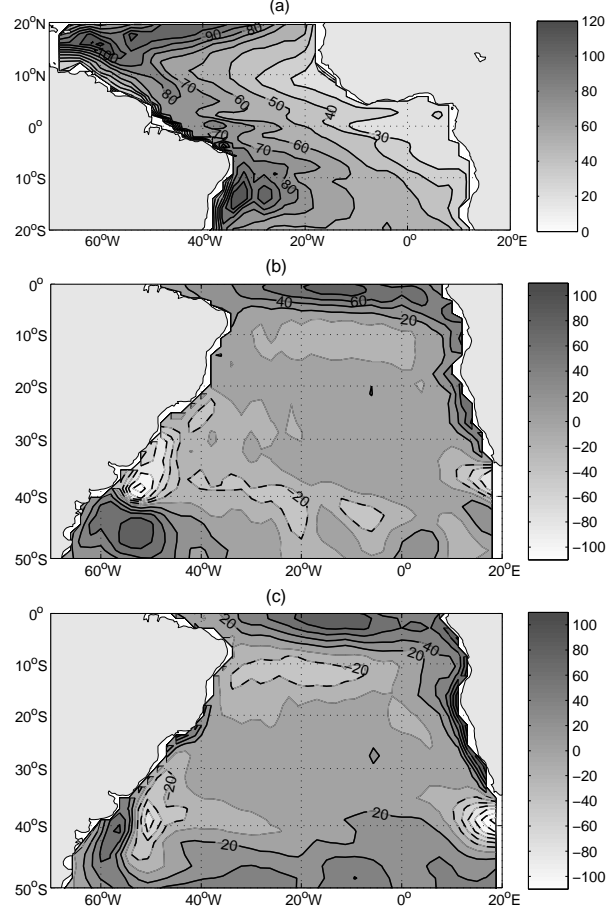


Figure 1: Annual mean of (a) ORCA2 thermocline depth, (b) the net heat flux as modelled by ORCA2 and (c) the net heat flux from NCEP/ NCAR reanalyses. Positive (negative) contour lines are solid (dashed), zero contour line is omitted, the contour interval is 10 [m] for (a) and 20 [Wm^{-2}] for (b) and (c).

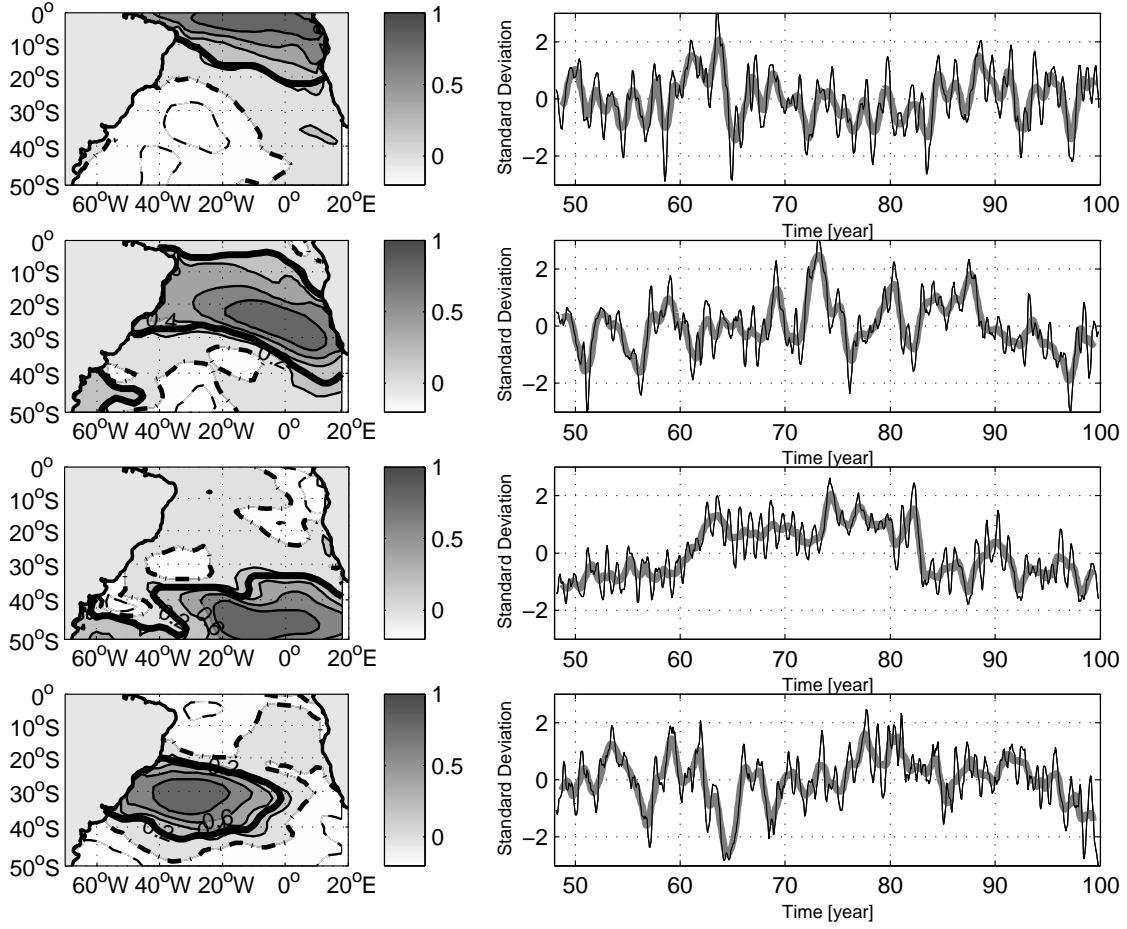


Figure 2: From top to bottom: First four rotated EOFs of ORCA2 MLT, left: Spatial pattern as homogeneous correlation maps, positive (negative) contour lines are solid (dashed), zero contour line is dashed - dotted, the contour interval is 0.2, right: Corresponding time series normalized by their standard deviation. The raw time series is shown in black. The thick grey line represent the time series smoothed with a one year running mean. Significant regions (95% significance interval) are within the thick line in the spatial plot.

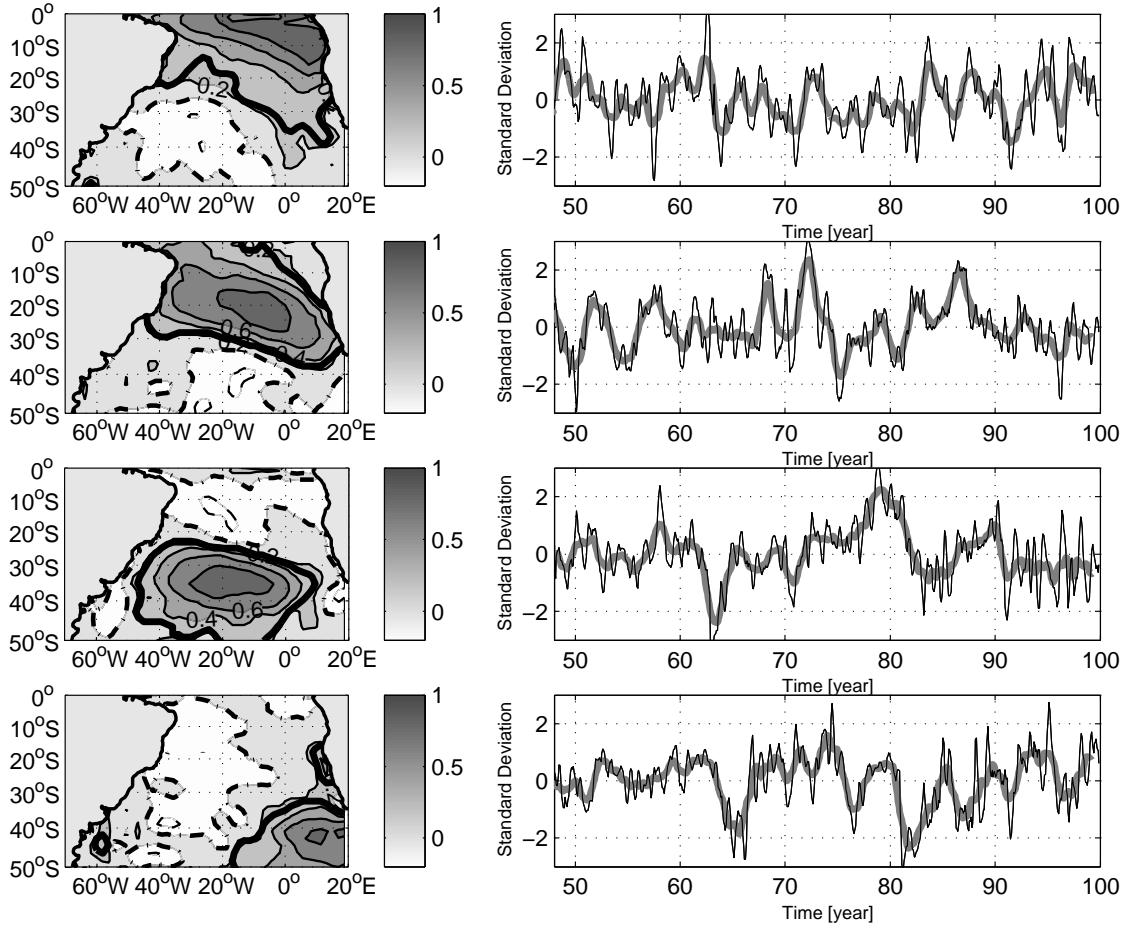


Figure 3: From top to bottom: First four rotated EOFs of NCEP/ NCAR SST. Left: Spatial pattern as homogeneous correlation maps, positive (negative) contour lines are solid (dashed), zero contour line is dashed - dotted, the contour interval is 0.2. Right: Corresponding time series normalized by their standard deviation. The raw time series is shown in black. The thick grey line represent the time series smoothed with a one year running mean. Significant regions (95% confidence interval) are within the thick line in the spatial plot.

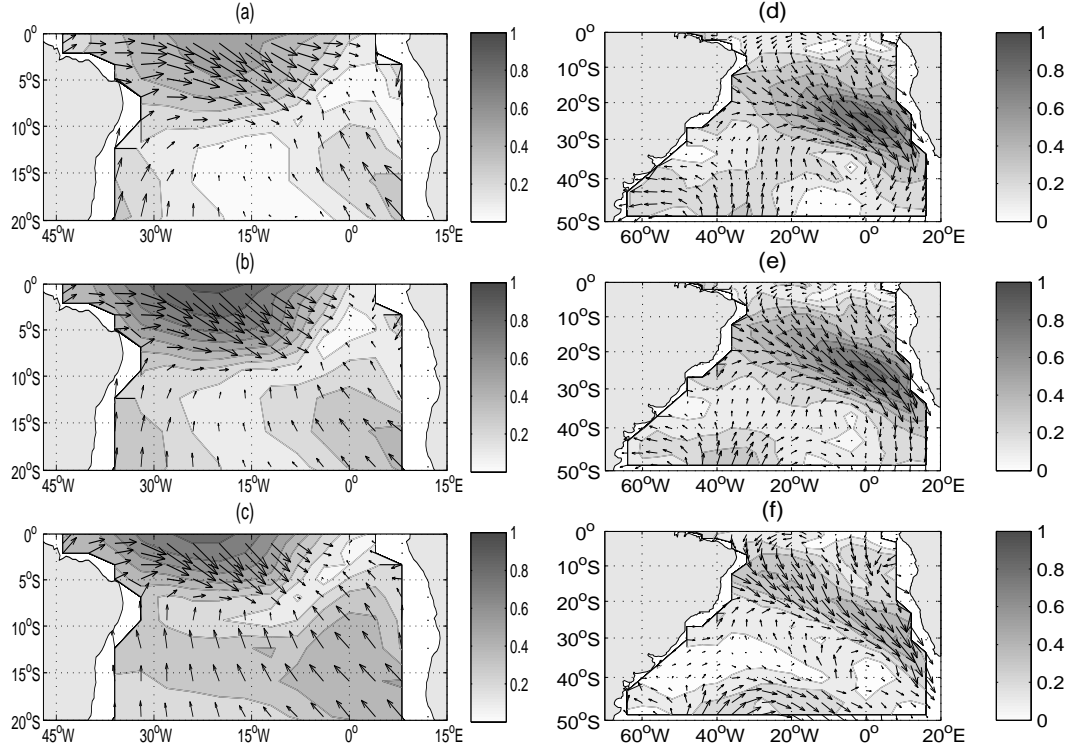


Figure 4: Sequences of lagged correlation between windstress and the first two REOF(MLT). Upper panel: *lead* = 3months, middle panel: *lag* = 0, and lower panel *lag* = 3months. Lead means REOF(MLT) leads the forcing field and lag means REOF(MLT) lags the forcing field.

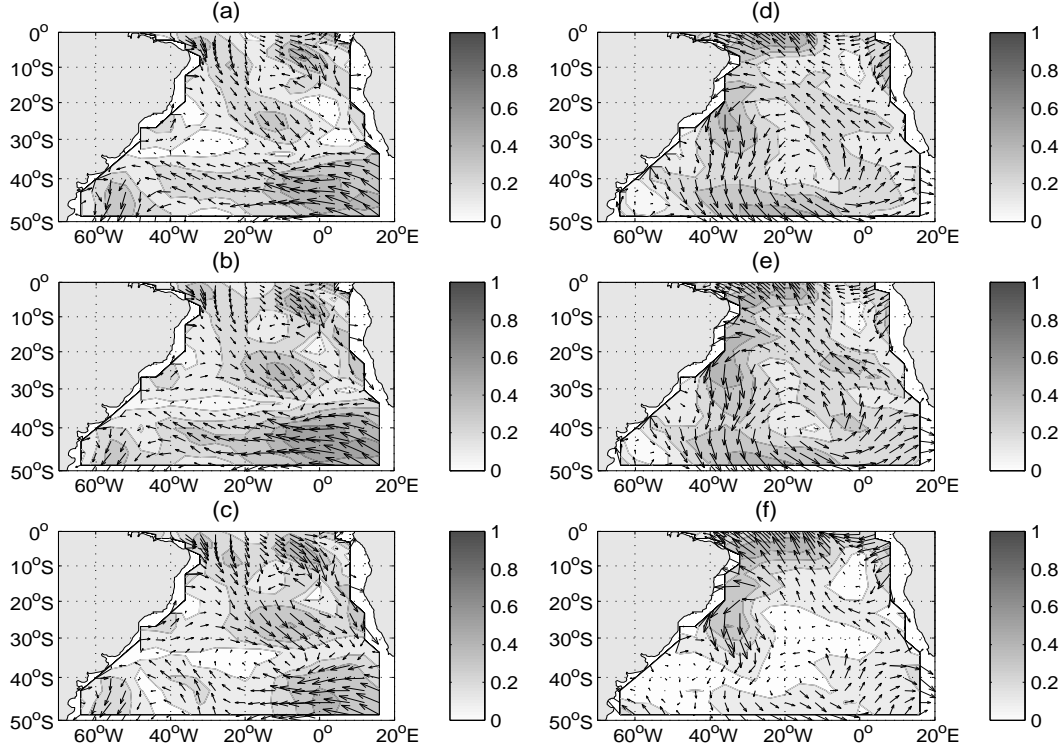


Figure 5: Sequence of lagged correlation between windstress and the third and fourth REOF(MLT). Upper panel: *lead* = 3months, middle panel: *lag* = 0, and lower panel: *lag* = 3months. Lead means REOF(MLT) leads the forcing field and lag means REOF(MLT) lags the forcing field.

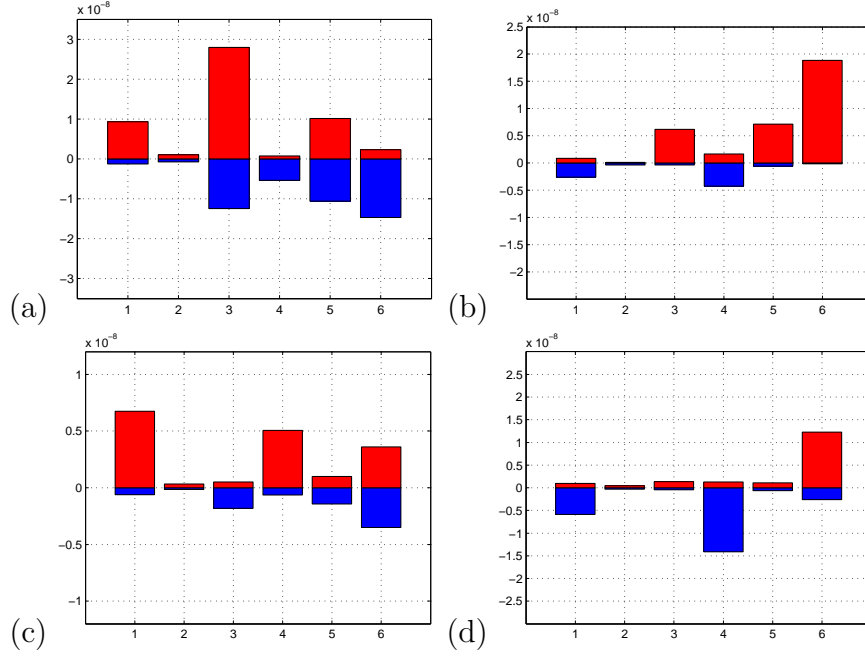


Figure 6: Bar diagram of the lagged regression analyses between the forcing terms in the temperature tendency equation (2) and the first four REOF(MLT). Bars correspond from left to right: (1) $-\mathbf{v} \cdot \nabla T$, (2) $\frac{\Delta T}{h} \mathbf{v} \cdot \nabla h$, (3) $-\frac{\Delta T}{h} w_h$, (4) $-\frac{\Delta T}{h} \frac{\partial h}{\partial t}$, (5) $-\frac{\overline{w'T'}}{h}$, and (6) $\frac{Q_{sfc}^{net}}{\rho c_p h}$. See text for details.

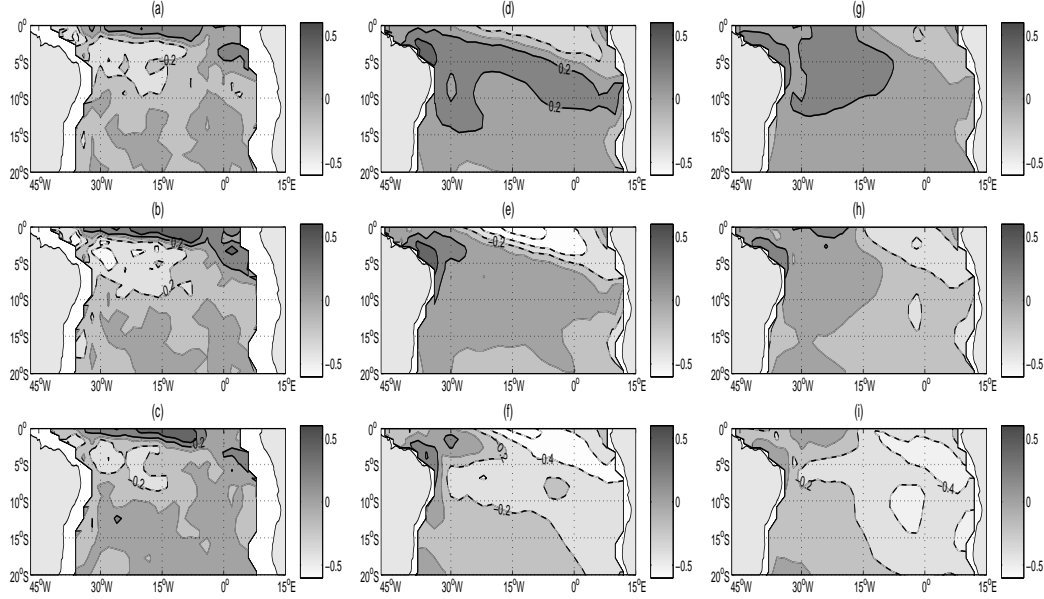


Figure 7: Sequence of the lagged correlation between the first REOF(MLT) and $-\frac{\Delta T}{h}w_h$, (left), Q_{sfc}^{net} (middle) and latent heat flux (right). Upper panel: *lead* = 3months, middle panel: *lag* = 0, and lower panel: *lag* = 3months. Lead means REOF(MLT) leads the forcing field and lag means REOF(MLT) lags the forcing field. Positive (negative) contour lines are solid (dashed). The zero contour line is dashed - dotted. The contour interval is 0.2.

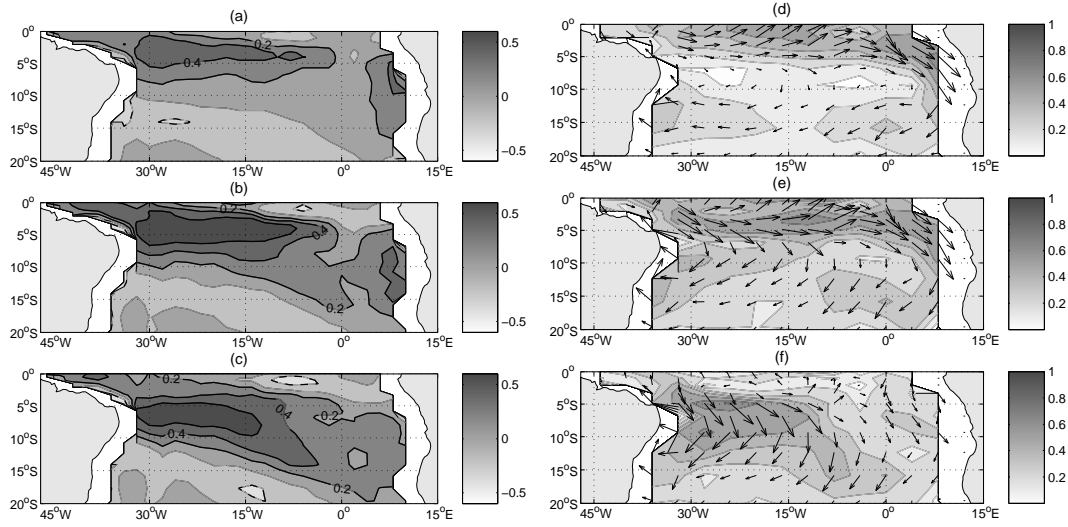


Figure 8: Sequence of the lagged correlation between the first REOF(MLT) and $-\mathbf{v} \cdot \nabla T$ (left) and \mathbf{v} (right). Upper panel: *lead* = 3months, middle panel: *lag* = 0, and lower panel: *lag* = 3months. Lead means REOF(MLT) leads the forcing field and lag means REOF(MLT) lags the forcing field. Positive (negative) contour lines are solid (dashed). The zero contour line is omitted. The contour interval is 0.2.

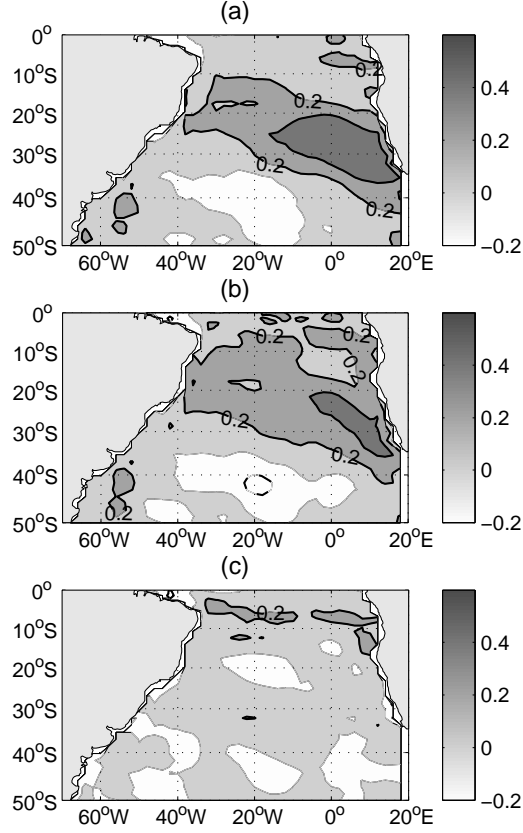


Figure 9: Sequence of the lagged correlation between the second REOF(MLT) and $\frac{Q_{sfc}^{net}}{\rho c_p h}$. Upper panel *lead* = 3*months*, middle panel: *lag* = 0, and lower panel: *lag* = 3*months*. Lead means REOF(MLT) leads the forcing field and lag means REOF(MLT) lags the forcing field. Positive (negative) contour lines are solid (dashed). The zero contour line is omitted. The contour interval is 0.2.

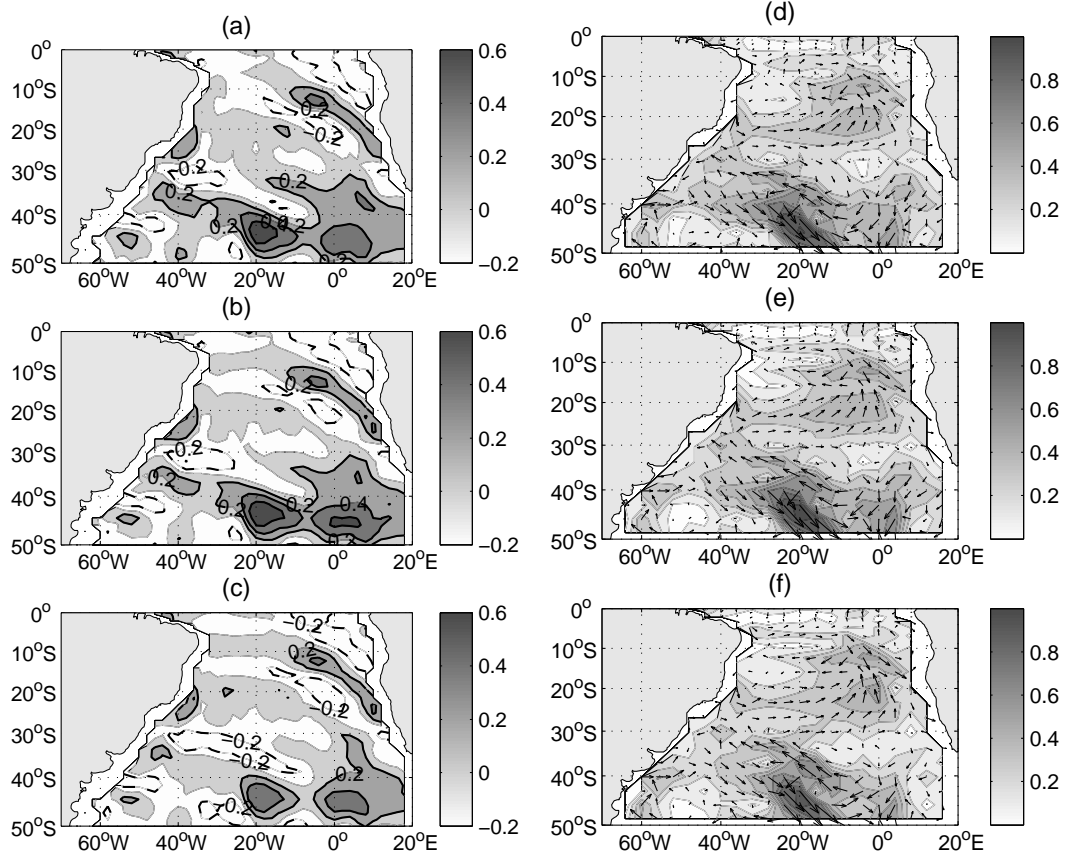


Figure 10: Sequence of the lagged correlation between the third REOF(MLT) and $-\mathbf{v} \cdot \nabla T$, and \mathbf{v} . Upper panel: *lead* = 3months, middle panel: *lag* = 0, and lower panel: *lag* = 3months. Lead means REOF(MLT) leads the forcing field and lag means REOF(MLT) lags the forcing field. Positive (negative) contour lines are solid (dashed). The zero contour line is omitted. The contour interval is 0.2.

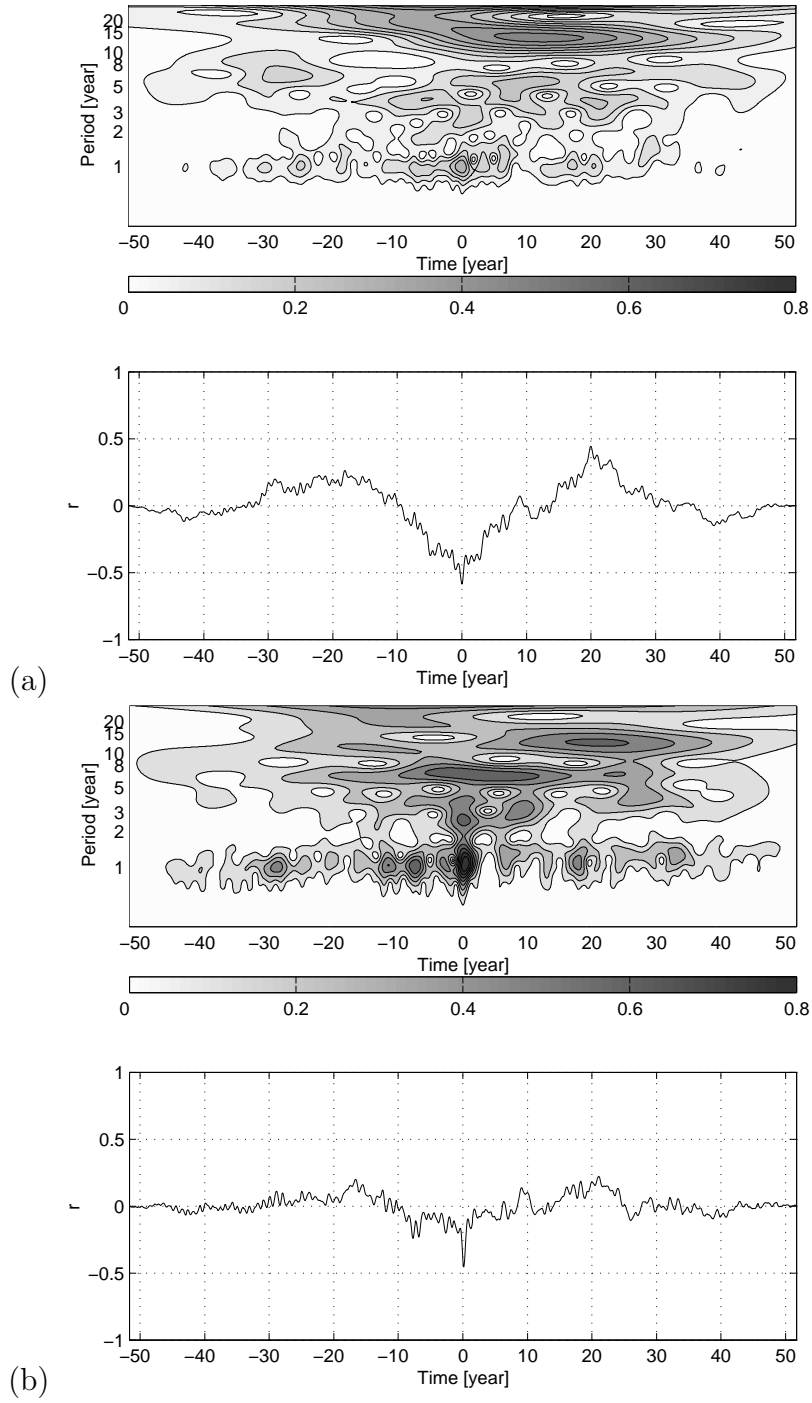


Figure 11: (a) Wavelet plot (upper) of the lagged correlation sequence (lower) between the third REOF(MLT) and meridional geostrophic velocities averaged over the region 10-20°W and 40-50°S, (b) as for (a) but for meridional Ekman velocities averaged over the region 0-10°E and 40-50°S.

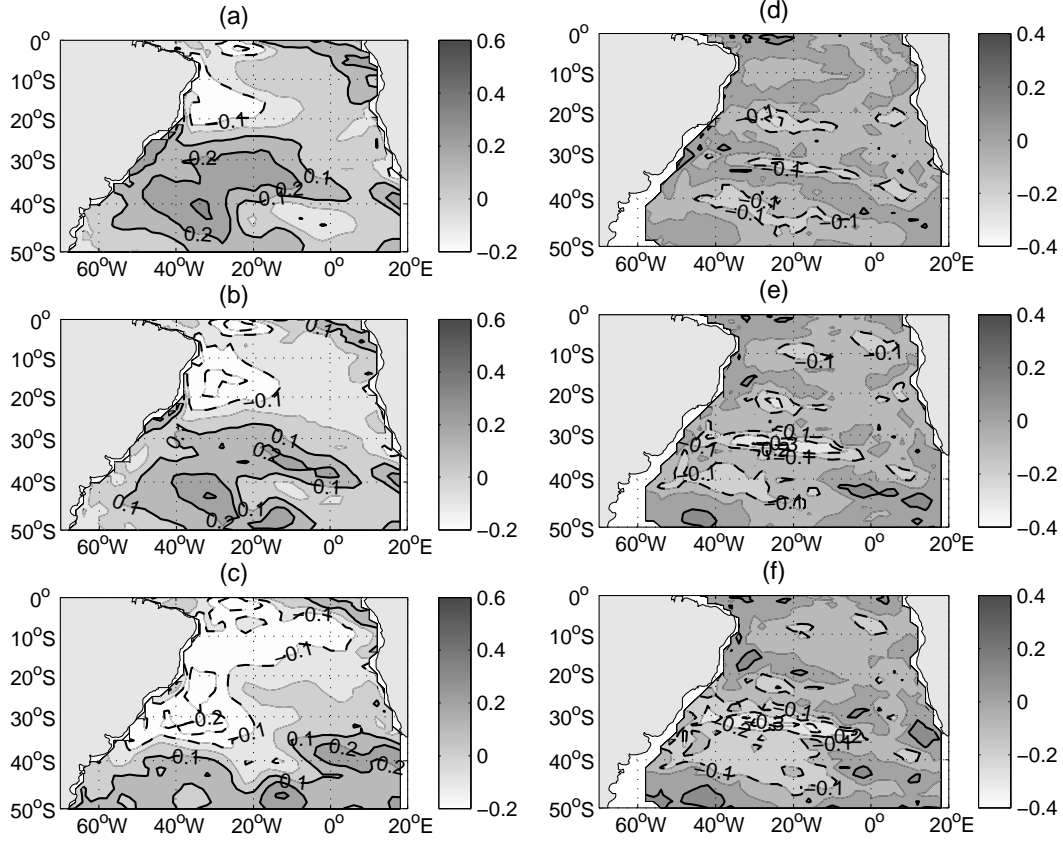


Figure 12: Sequence of the lagged correlation between the fourth REOF(MLT) and Q_{sfc}^{net} , and $-\frac{\Delta T}{h} \frac{\partial h}{\partial t}$. Upper panel: *lead* = 3months, middle panel: *lag* = 0 and lower panel *lag* = 3months. Lead means REOF(MLT) leads the forcing field and lag means REOF(MLT) lags the forcing field. Positive (negative) contour lines are solid (dashed). The zero contour line is omitted. The contour interval is 0.2.

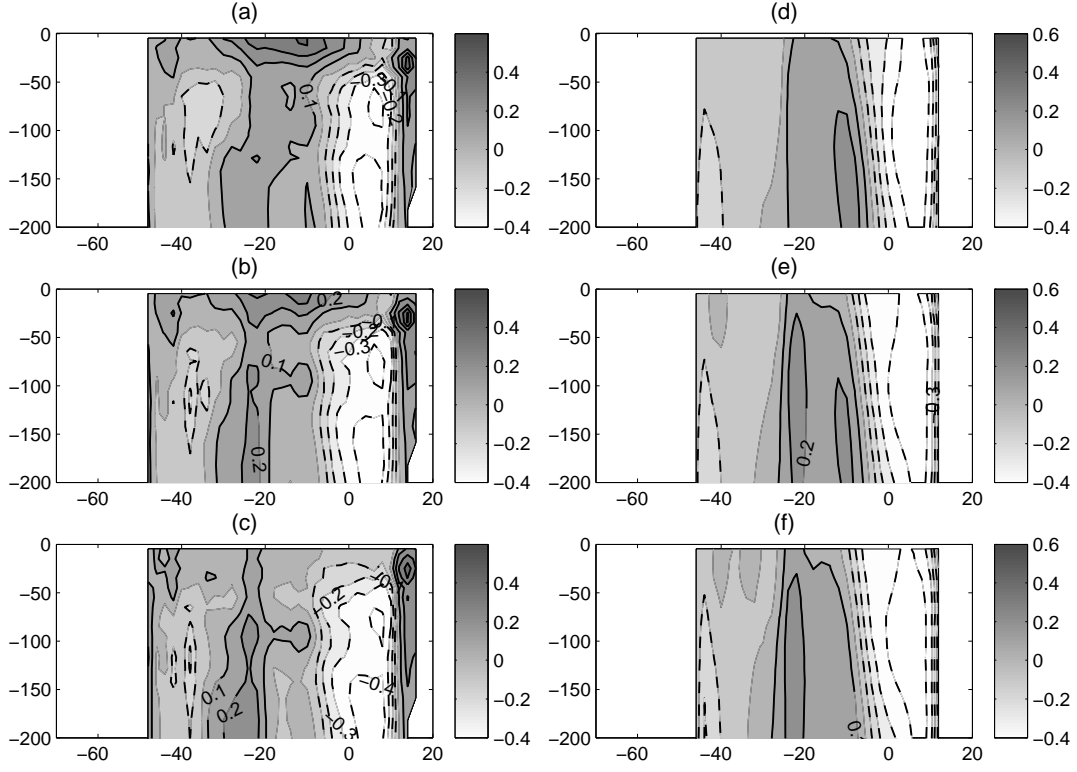


Figure 13: Sequence of vertical section of correlation between the second REOF(MLT) and heat transport anomalies through 30°S . The transport has been calculated using total model velocities (left) and geostrophic velocities (right). Upper panel: *lead* = 3months, middle panel: *lag* = 0, and lower panel: *lag* = 3months. Lead means REOF(MLT) leads the forcing field and lag means REOF(MLT) lags the forcing field. Positive (negative) contour lines are solid (dashed). The zero contour line is omitted. The contour interval is 0.1.

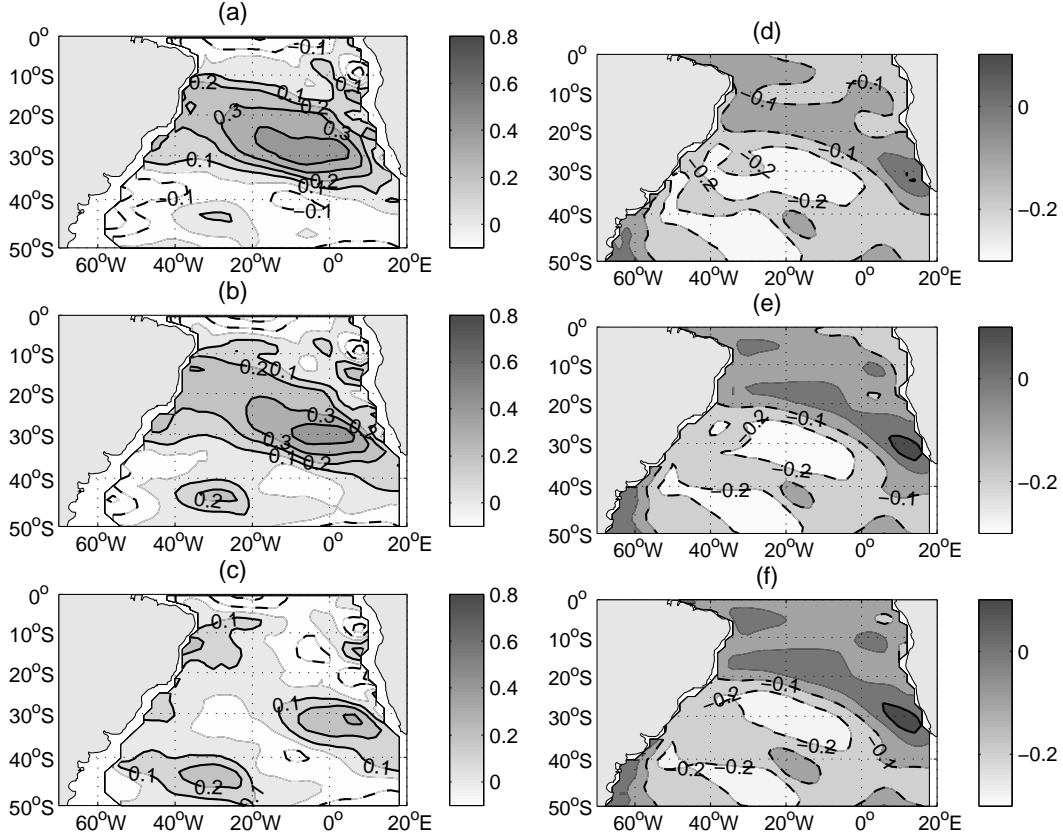


Figure 14: Sequence of the lagged correlation between the second REOF(MLT) and the meridional Ekman heat transport (left) and SSH anomaly (right). Upper panel: *lead* = 3*months*, middle panel: *lag* = 0, and lower panel: *lag* = 3*months*. Lead means REOF(MLT) leads the forcing field and lag means REOF(MLT) lags the forcing field. Positive (negative) contour lines are solid (dashed). The zero contour line is omitted. The contour interval is 0.1.